The Spatial and Temporal Probability of Dust Storm Activity in Chryse, One of the Tentative Landing Areas of Tianwen-1 Mission

Bo Li (libralibo@sdu.edu.cn)
Shandong University
Jiang Zhang
Shandong University
Zongyu Yue
Chinese academy of sciences
Peiwen Yao
Shandong University
Chenfan Li
Shandong University
Biao Wang
Shandong University
Xiaohui Fu
Shandong University
Zongcheng Ling
Shandong University
Shengbo Chen
Jilin university

Full paper

Keywords: Tianwen-1 mission, the Chryse area, dust storm, EOF analysis, preferred landing areas

Posted Date: July 20th, 2020

DOI: https://doi.org/10.21203/rs.3.rs-41993/v1

Abstract

Dust storms, observed in all seasons, are among the most momentous Mars atmosphere activities. The Entry-Descent-Landing (EDL) activity of a Martian landing mission is influenced by local atmospheric conditions, especially the dust storm activity probability. It is of great significance to know well the dust storm situation that China's first Mars mission (Tianwen-1) may encounter in EDL season in the Chryse area, one of the tentative landing areas. Firstly, based on four Martian years' Mars Orbiter Camera (MOC) Mars Daily Global Maps (MDGMs), 1172 dust storms were identified within Chryse's 1600 km radius ring with their shape parameters extracted, including center, range and area. Secondly, the daily mean dust storm probability was calculated binned by 1° of solar longitude in the Chryse area during EDL season. Dust storm activity frequency was closely interrelated with the seasonal ebb and flow of the arctic polar ice cap, consequently, most of dust storms occurring in either the cap's grow or the recession. The dust storm activity in the Chryse area mainly came from the northern polar cap region, Acidalia and Chryse, with some contribution from the southern hemisphere (Argyre and Bosprous) northward. Thirdly, we divided the Chryse area into many square grids of 0.5° and computed the average occurrence probability of dust storm in each grid during EDL season. The dust storm activity probability in space was also in-homogeneous, low in the west and south but high in the east and north, which was mainly affected by three factors: topography, the origin and the path of dust storm sequence. Based on Empirical orthogonal function (EOF) analysis, of the storms in the Chryse area we've discovered, 40.5% are cap-edge storms in the northern hemisphere and 17.5% are textured dust storms. Finally, according to the temporal and spatial probability of dust storm activity in the Chryse area during EDL season, we held that the preferred landing time of the Tianwen-1 mission in 2021 was in Ls=18°-65° and three preferred landing areas were selected with low dust storm probability.

1 Introduction

The atmospheric pressure on Mars is 1% less than Earth's, but Mars is not short of dynamics. Dust storms, observed in all seasons, are one of the most momentous Mars atmosphere activities in both spacecraft and Earth-based observations (Gifford, 1964; Peterfreund and Kieffer, 1979; Zurek and Martin, 1993; Cantor et al., 2001; Cantor, 2007). Dust storms on Mars show great variability in time and space with strong radiation activities (Heavens et al. 2011) ranging from local to global. According to previous Earth-based and spacecraft observations, three significant characteristics of the Martian climatic system have been revealed: (1) the models of seasonal polar cap's growth and decline in mass recurring year after year (Cantor et al., 1998; James and Cantor, 2001); (2) the large-scale local and global dust storms expanding stochastically to a greater or lesser extent in the period of half year known as the typical "dust storm season" (Martinand Zurek, 1993); (3) the preferred origin regions of dust storms (Acidalia, Utopia, Arcadia, Hellas, etc.) locating in both southern and northern hemispheres (Wang et al., 2015).

The China's first Mars probe mission (Tianwen-1) is scheduled to be launched in 2020 with the goals of "orbiting, landing and roving" (Ye et al., 2017). It will carry out detailed investigations of landing areas by rover patrolling exploration with a high accuracy and resolution. In order to select safe landing areas,

several factors (such as topographic slope, latitude, geographic elevation, coverage of dust, distribution of rocks, local wind speed and visibility) were taken into account and two tentative landing areas (Chryse and Isidis) were chosen in the latitude range of 5°-30° (Fig. 1a).

The dust storm activity probability in space and time in tentative landing areas is also a key to Martian landing area selection in addition to the above factors. Dust storm activity can affect the precision and success during Entry-Descent-Landing (EDL) season for a Martian landing mission (Ryan and Henry, 1979; Smith, 2004; Vasavada et al., 2012). The Spirit and Opportunity rovers landed just in the summer dust storm season in Mars southern hemisphere, causing their landing sites to be 10.1 km and 24.6 km away from the center of the landing ellipses (Desai and Knocke, 2007). MSL, a Mars mission, evaluated the dust storm activity probability in the landing area of EDL season (near Gale Crater) in advance with the result that the landing position was only 2.4 km away from the center of the landing ellipse (Martin-Mur et al., 2012).

It is known that Isidis, one of the tentative landing areas of Tianwen-1 mission, is close to the Syrtis and Jezero sites of NASA Mars 2020 Rover mission (Fig. 1a). Cantor et al. (2019) employed MRO MARCI images (MY 28-MY 34) to look into dust storm activity within a 2000 km radius of Syrtis and the Columbia Mountains and found that the dust storm activity probability was about 1.6% in the Colombian mountains and 3.2% in the Syrtis site. Hence, this paper tends to study the dust storm activity probability in space and time, in the Chryse area and within its 1600 km radius monitoring ring. According to previous works (Wang et al., 2015), Chryse is an important dust storm activity origin area in the northern hemisphere of Mars, and it lies to the south of Acidalia and the north of Argyre (Fig. 1a). Acidalia and Argyre are also the dust storm's origin areas, of which Acidalia is the one where dust storm sequence occurs most intensively. Moreover, there are two dust storm sequences passing through the Chryse area. One comes from Acidalia travelling to the south, and the other comes from the Argyre travelling to the north (Wang et al., 2015). It is meaningful for us to focus on dust storms during EDL season for the Chryse area in time and space. Therefore, it's critical to China's 2020 Mars Mission to detect the possibilities and characteristics of dust storm activities in and around Chryse by aid of remote sensing imagery collected over multiple Martian years.

In this paper, we used the images of Mars Orbiter Camera (MOC) onboard the Mars Global Surveyor (MGS) to: (1) identify the dust storms within Chryse's 1600 km radius ring and extract their shape parameters such as center, range and area; (2) calculate the daily mean dust storm probability within Chryse's 1600 km radius ring binned by 1° of solar longitude; (3) divide the Chryse area into many square grids of 0.5° and compute the mean occurrence probability of dust storm in each grid during EDL season and a Martian year; (4) employ Empirical orthogonal function (EOF) analysis to find out the leading and separate dust occurrence in space on 0.5 degree grids in the Chryse area and the seasonal cycle.

2 Data And Methods

2.1 MOC Mars Daily Global Maps

MGS was the first successful NASA mission launched to Mars since the Viking mission in 1976 and went silent in November, 2006. The MGS MOC aimed at acquiring daily global images to study the temporal and spatial models of the Martian atmosphere over the course of one Martian year (Malin et al., 1992). MGS has made a lot of observation achievements since its launch, one of which is that it has been confirmed that there was water on Mars in ancient times, such as an ancient Delta and valleys and wall gullies formed after the current. The MGS MOC science investigation used 3 instruments: two wide-angle (WA) cameras with red (580–620 nm) and blue (400–450 nm) band passes (WAR and WAB), whose maximum resolution is ~ 230 m/pixel and a narrow-angle camera for obtaining gray (black and white) high-definition images (usually 1.5 to 12 meters per pixel). Each WA camera contains a single linear CCD array (3456 pixels across) with a “fish-eye” lens providing a 140° field-of-view. The WA cameras provide the planetary edge view from 12:17 to 15:43 LMST with an intrinsic resolution of about 230 m^{-1} at the lowest point and 1.5 km^{-1} at the edge (Malin et al., 1992). MOC has sent back more than 2.4 million images spanning 4.8 Martian years’ portions. With their "daily global map" mode running, the WA camera continuously maps the Mars surface at a constant resolving power of 3.75 or 7.5 km per pixel. The Mars daily global map (MDGM) is a global image mosaic with 13 single MOC wide-angle mapping blocks, covering about a complete Mars day (Wang and Ingersoll, 2002). The MDGMs have a resolution of 0.1°×0.1° (~ 6 km/pixel at the equator), which were archived in 4 mission sub-phases and can be downloaded from website http://marsclimatecenter.com/data/mocbrowse/.

2.2 Dust storm detection

In MOC MDGMs, the Martian surface covered by dust storms shows yellow color, while the exposed rocks usually show black color (Fig. 2a). As a result of atmospheric dynamics, the Martian surface covered by meteorological phenomena such as dust storms and clouds shows white color or has visible structures (Fig. 2). In this paper, dust storms were identified in accord with the visual detection procedure described in detail in Cantor et al. (2001). Condensate clouds (ice) have a higher single-scattering albedo than dust storm in the WAB band pass of MOC, so it is more equably white (James, 1985) and brighter at blue bands than red bands (black arrows in Fig. 2b and c). The opposite is true for dust storm (white arrows in Fig. 2b and c). We could discriminate between dust storms and condensation clouds by force of the contrast between WAR and WAB images of the same MOC.

In light of the above-mentioned dust storm detection methods, 1172 dust storms were identified within the 1600 km radius monitoring ring in the Chryse area with the support from four Martian years' MOC MDGMs. Then each identified dust storm was vectorized as a polygon feature with the GIS software and its shape parameters were extracted and measured, including center, area and range. Lambert Conformal Conic Projection was adopted to reduce the projection deformation, ensuring these measurements accuracy. This projection was based on the GCS_Mars_2000 (a geographic coordinate system) whose datum is the D_Mars_2000.

2.3 Planet encircling dust event

There was only one planet encircling dust event (PEDE) in the four Martian years' investigations of MGS, starting at Ls = 184.7° in MY 25 (26, June 2001) and receding around Ls = 200.4°, with duration time of 120 sols or so (Cantor et al., 2007). By 2019, only seven confirmed PEDEs have been observed (Shirley and Mischna, 2017), occurring in 1956 (Miyamoto, 1957; Martin and Zurek, 1993; Zurek and Martin, 1993), 1971–1972 (Martin, 1974), 1973 (Martin, 1976), two in 1977 (Briggs et al., 1979; Ryan and Sharman, 1981; Zurek and Martin, 1993), 2001 and 2018. However, we still know a little about PEDE up to now. In line with the predecessors' observations, two characteristics of PEDE have been revealed: (1) the onset of PEDE usually occurred in the southern spring and summer seasons (Ls = 204°-300°) (Zurek and Martin, 1993); (2) PEDEs were observed to originate in three main areas: the northwest of Hellas, the west, the south, and the southeast of Solis Planum and Claritas Fossae, and Isidis (Cantor, 2007). Chryse region is not within the above three ones, and the Tianwen-1 mission's EDL season isn't in the period Ls = 204°-300°. As a non-universal phenomenon, dust storms in PEDE will produce deviation in determining the spatial and temporal probability of dust storm activity in the Chryse area. Therefore, the dust storms, happening in PEDE of 2001, were not considered and identified in this paper.

3 Temporal Probability Of Dust Storm Activity In Chryse

Dust storm events have seasonal patterns, which recur year after year, thus it is reasonable for us to estimate the dust storm activities in EDL season (Tamppari et al., 2008; Vasavada et al., 2012). Hence, it is extremely vital to understand the dust storm probability of Tianwen-1 mission in EDL season expecting to improve the landing safety and accuracy for the landing mission success.

3.1 Dust storm activity of a Martian year round

The daily mean probability of dust storm activity is an extremely significant factor to Mars landing probe, due to its function of improving landing accuracy, which may be affected by severe conditions such as strong winds and dust storms (Vasavada et al., 2012). The daily mean probability $P(A)$ of dust storm activity can be given by (Cantor et al., 2019):

1

In Eq. (1), i is the index of the four Martian years in MGS MOC observations, $N(i, d)$ is the number of dust storms identified on a sol (d) of the given Mars year (i), $A(i, d)$ is the total dust storm area identified on a sol (d) of the i Mars year divided by the whole study area, which is the percentage of dust storm area on the sol (d) of the i Mars year. Four Martian years in total, $n(d)$ is the sum of dust storms identified on the same sol of four Martian years. This paper has corrected the partial area coverage of each storm and the probabilities of the all MOC observations. The higher the value of $P(A)$ is, the larger the daily coverage of dust storm in monitoring area is. However, the probability of dust storms recurring in the same sol was

not taken into account or reflected in Eq. (1). Taking two arbitrary sols, sol 1 and sol 2, as an example, there are dust storms in sol 1 in all four Martian years, but the area of these dust storms is small. $P(A)$ of sol 1 is the average percentage of dust storms in four years. While in sol 2, dust storms occur only in one Martian year, but the area of dust storms is large. It is unreasonable that probability of dust storm activity in sol 1 is larger than that of sol 2. In this paper, the probability $P(d)$ of dust storms recurring on the same sol (d) in four Martian years can be given by:

2

where $Is(i, d)$ indicates whether there is a dust storm on sol (d) of Martian year (i). If dust storms occur on sol (d) of Martian year (i), the $Is(i, d)$ is 1; while there is no dust storm, the $Is(i, d)$ is 0. According to Eqs. (1) and (2), the daily mean probability $P(d, A)$ of dust storm (considering both time probability and area probability) is as follows:

3

According to Eq. (3), the daily mean dust storm activity probability in the Chryse area and within its 1600 km radius ring is shown in Fig. 3 in line with 1172 dust storms observed during MY 24–28.

(1) As shown in Fig. 3, Adp_ds in the Chryse area showing blue color and within its 1600 km radius ring showing red color peaked at 42.9% with Ls = 223° and 20.9% with Ls = 225°, respectively. The minimum of Adp_ds in Chryse and within its 1600 km radius ring was 0. For example, during Ls = 39°-72°, no dust storm was identified in the four Martian years' MOC MDGMs in the Chryse area. Adp_ds in the Chryse area and within its 1600 km radius ring was one order of magnitude higher than that (the maximum was 5%) calculated by Cantor et al. (2019) at candidate landing sites for NASA Mars 2020 Rover mission. The four Martian years' MOC MDGMs at Ls = 223° in the Chryse area were shown in Fig. 4. At Ls = 223° of MY 24 and MY 27, dust storms almost covered the whole Chryse area (Fig. 4a and d). While at Ls = 223° of MY 25, the dust storms were excluded because of the PEDE; and at Ls = 223° of MY 26, there was no dust storm in the Chryse area (Fig. 4b and c). As a result, it was reasonable to make a conclusion that the Chryse area had a large Adp_ds (42.9%) at Ls = 223° for MY 24–28. In addition, Adp_ds in the Chryse area was higher than that within its 1600 km radius ring at the same sol, which may be caused by the fact that the area of the latter (8.04×10^6 km^2) is larger than that of the former (6.20×10^6 km^2).

(2) Adp_ds in the Chryse area and within its 1600 km radius ring showed obvious in-homogeneity and seasonality within a Martian year. In the Chryse area, dust storm activity was the most frequent from the northern hemisphere autumnal equinox (Ls = 177°) to the end of autumn (Ls = 239°), with an average Adp_ds of 9.5%. Another period with high Adp_ds in the Chryse area was from the northern hemisphere

winter solstice (Ls = 288°) to the next spring (Ls = 4°) on Mars, with an average Adp_ds of 4.1%. The active period of these two dust storm activities within Chryse's 1600 km radius ring was longer than those in the Chryse area. Their duration ranged from Ls = 152° to 247° and from Ls = 269° to Ls = 92° with their mean Adp_ds of 2.9% and 1.0%, separately. This was not due to the study area's growth, but the northward movement of the 1600 km radius ring near the seasonal cover edge in the northern hemisphere, where dust storms occurred frequently (Cantor et al., 2001; Cantor, 2007; Cantor and Malin, 2007). Moreover, a small number of dust storms occurred during Ls = 93°-123° within Chryse's 1600 km radius ring.

(3) The green curve shows the average optical depth provided by the Spirit Rover during the mission, with increments of 2.5° Ls, eliminating the responses of the PEDE in MY 29 (Lemmon et al., 2015). The average optical depth peaked at 1.0 (Ls = 160°), 1.2 (Ls = 240°) and 1.45 (Ls = 330°), respectively. The elevated optical depth obtained by the rover was related to storm activity observations in the Chryse area and its 1600 km radius ring, except for the first peak (Ls = 160°) (Fig. 3). Chryse and the Spirit Rover were located in different parts of Mars (far away from each other), but the dust storm curves and optical depth obtained from them were similar in laws and shapes. Dust storms at the end of summer in the northern hemisphere (Ls = 160°) mainly occurred at the edge of the Antarctic cap that recedes seasonally, while the edge of the Arctic cap recedes toward the north pole of 75° N. Spirit Rover located in the southern hemisphere of Mars (14.6° S) and was closer to the south polar cap edge than the Chryse area, which would be easily affected by the storms from the south polar cap edge around Ls = 160°. However, the Chryse area was far away from both south and north polar caps at Ls = 160° and there was nearly no dust storm.

(4) Dust storm activity in both Chryse and within its 1600 km radius ring was mainly centered during the period from Ls = 180° to Ls = 240°. We deemed that these storms were resulted from the Acidalia-Chryse channel of dust storm. Acidalia-Chryse channel was the most common development mode of dust storm sequences and each sequence propagated along the same path repeatedly, lasting for 5-plus sols. It seemed to have a bearing on frequent frontal eruptions (or "pumping" of storms by frontal systems) in high latitudes of the northern hemisphere. In each sol, one or more dust storms appeared in the Acidalia-Chryse channel during Ls = 214°- 228° in MY 27 (Wang et al., 2015).

3.2 Latitudinal distribution of dust storms within Chryse's 1600 km radius ring

In order to study the relationship between location (latitude) and time of dust storm occurrence within Chryse's 1600 km radius ring, we have made a 2D scatter map which took the central latitude and sol of dust storm activity as the Y and X axis (Fig. 5).

The latitude of Chryse's 1600 km radius ring ranges from 60° N to 20° S, where the center of dust storm identified in this paper is located. Major storm activity in the Chryse monitoring area was ongoing early in the Martian year (Ls = 0°), originating along the arctic cap edge, the north of the Chryse, which recedes seasonally. From Ls = 0°-90°, as the dust storm centers gradually moved northward, the dust storm in

south of the Chryse would gradually disappear with the seasonal arctic cap edge having receded poleward of 83° N. As Ls increased, the quantities of dust storms decreased by degrees until Ls = 90° where dust storm can no longer be observed in the monitoring area. From the beginning of the northern summer solstice (Ls = 90°) to Ls = 130°, the northern hemisphere dust storm activity disappeared in the Chryse area, only once near the equator. We held that there was no dust storm activity in the Chryse's 1600 km area at the end of the northern spring, which may be caused by: (1) a longitudinal offset in Acidalia storm zone (Hollingsworth et al., 1997), where the northern hemisphere spring dust storm activity is initiated; (2) the continued northward regression of the arctic polar cap edge, followed by most Martian storms (Cantor et al., 2001; Cantor and Malin, 2007; Guzewich et al., 2017); (3) the minimum period of storm activity in most parts of the Mars (including Chryse) is regarded as the solstice minimum (Ls = 90°). As storm activity recurred around mid-summer (Ls = 135°), some of the storms have transferred to the southern hemisphere, starting from the northern Argyre and Bosporus Straits during Ls = 135 °- 160° (Fig. 6a). These storms moved north toward the south of the Chryse area, but with their small size and little impact range (Fig. 6b and c).

The storm activity is becoming active in the Arctic and Chryse regions with the North autumnal equinox (Ls = 180°) arriving and the seasonal arctic cap edge expanding. During Ls = 180°-250°, the scale and range of dust storm activity gradually increased, as it moved southward. Most of dust storm activities came from the Chryse area or its north, observed in MOC MDGMs of four Martian years. There were not only native dust storms (white arrows in Fig. 7) originating in the Chryse area, but also multiple frontal/flushing dust storms (black arrows in Fig. 7) moving along the Acidalia cross-equatorial storm-track (green arrows in Fig. 7) (Wang et al., 2005; Wang, 2007). Only three dust storms were located in the southern hemisphere of Mars. As the seasonal arctic cap edge had grown towards the equator of 55°N at the end of northern autumnal season (Ls = 250°-280°), the frequency and scope of dust storm activity reached to the minimum. About half a month after the winter solstice in the northern hemisphere (Ls = 270°), dust storm activities would recur in the monitoring area, mainly distributing at the edge of the arctic cap and the north of Chryse. There were also some small-scale dust storms in the southern hemisphere, probably starting from Argyre and Bosprous. These Chryse and arctic polar cap edge storms will last from Ls = 270° to the next Martian year, respectively.

The latitudinal distribution of dust storm center in the monitoring area with the criterion of Ls = 1° (Fig. 5) showed seasonal and spatial heterogeneity. Firstly, the dust storm activity frequency was closely related to the seasonal waxing and waning of the arctic polar ice cap. Dust storms within Chryse's 1600 km radius ring mostly arose during the rise or the decay of the polar cap rather than its quiescent stage when the cap's change rate approached to the minimum. In the northern hemisphere, the dust storm activity at the edge of cap almost was at a standstill before or on the North Summer Solstice, and this stagnation lasted for a long time (Ls = 20°-90°). Secondly, the dust storm activity within the monitoring area mainly came from the Arctic Polar cap, Acidalia and Chryse, and a small numbers arose from the southern hemisphere (Argyre and Bosprous) northward. Nevertheless, the dust storms from the southern hemisphere are much smaller and much less frequent than the ones from the northern hemisphere.

3.3 Dust storm probability during the EDL season

Tianwen-1 mission is consisted of five phases (Ye et al., 2017): Earth-Mars transfer stage, Mars orbit insertion stage, Mars orbit parking stage, Deorbit and landing stage and Scientific exploration stage. Tianwen-1 and NASA Mars missions in 2020 have the homologous launch window. Assuming that Tianwen-1 will be launched in July 2020, the same time as NASA's Mars 2020, the EDL season of China's Mars mission is about April June 2021 (MY 36, Ls = 25.1°-65.4°), which is different from that of NASA's Mars 2020 (Ls = 345°-25°). Consequently, this paper tends to set the EDL season as Ls = 345°-65° in combination with the Mars missions of China and NASA. According to Eq. (3), the Adp_ds during EDL season in Chryse and within its 1600 km radius ring were calculated and shown in Fig. 8.

(1) As shown in Fig. 8, Adp_ds from MOC MDGMs of MY 24-MY 28 in Chryse (blue color) area peaked at 30.6% (Ls = 348°) during EDL season. The dust storm activity in Chryse area is discontinuous by and large, but it is continuous in the range of Ls = 345°-3°, with an average Adp_ds of 4.8%. Afterwards, dust storm activity recurred from Ls = 13°-18°, but it was very weak with an average Adp_ds of 1.3%. As to dust storm activity within Chryse's 1600 km radius ring, the Adp_ds peak decreased to 3.9% at Ls = 3.8° continuing almost throughout the EDL season (Ls = 345°-49°) with an average Adp_ds of 0.9%.

(2) We deemed that the dust storm probability in the Chryse area during EDL season had a bearing on northward movement of storm activity on the edge of the Arctic polar as the seasonal arctic polar cap edge receded northward from 58°N to 65°N. During the warm season in the northern hemisphere (Ls = 345°-5°), the arctic polar cap began to melt and a great quantity of carbon dioxide was released into the Mars Atmosphere. As the arctic polar cap edge receded northward, the cap-edge storms occurred and prevailed by degrees. These cap-edge storms move southward through the Chryse area along the Acidalia storm-track (Wang et al., 2015). In late northern spring (Ls = 45°-80°), as it receded, the northern polar cap was far away from Chryse and the change rate of arctic polar cap size was near the minimum, thus the dust storm activity probability was lowest within Chryse's 1600 km radius ring .

(3) The success and accuracy during EDL season is decided by Chryse's atmospheric conditions, especially the dust storm activity probability. It would be best to finish the landing procedure during the period with lower Adp_ds in EDL season so as to reduce the risk. In EDL season, dust storm lasted during Ls = 345°-3° and 13°-18° in the Chryse area, which was not the time for landing mission. While during Ls = 18°-65°, dust storm activity was found in only five sols, the Adp_ds ranged from $\leq$ 1.6% with an average of 0.15%. The probabilities above mentioned were consistent with the estimate of MSL candidate landing site, which wss less than 3%, that was 0.1% for the actual Gale site (Vasavada et al., 2012), ranging from 1.6% in the Colombian mountains to 3.2% in the Syrtis site for NASA 2020 Mars mission (Cantor et al., 2019). We could come to a conclusion that dust storms will not give rise to major hazards to Ls = 18°- 65° in the EDL season of Tianwen-1 mission.

4 Spatial Distribution Of Dust Storm Activity In Chryse Area

The dust storm activity on Mars is characterized by obvious spatiotemporal heterogeneity. That means dust storm probability varies from different Martian surfaces. In this section, we studied the average spatial probability of dust storm activity in the Chryse area ascertaining the most suitable landing area. For sake of calculating the Asp_ds in different areas, the research area was divided into regular grid, each grid side length being 0.5° in this paper. The Asp_ds in each 0.5° grid in a whole Martian year can be calculated by:

4

While the Asp_ds in 0.5° grids during the EDL season can be calculated by:

5

Where $N(i, g)$ is the number of dust storms identified in a given grid (g) of the given Mars year (i), $A(i, g)$ is the total dust storm area identified in a given grid (g) of the given Mars year (i) divided by the given grid area, which is the percentage of dust storm area in a given grid (g) of the i Mars year. $n(g)$ is the total number of dust storms in the given grid (g) of four Martian years. Martian year and the EDL season can be divided into 36 and 9 segments binned by 10° of Ls, separately. s is the index of the segment, and $Is(s, g)$ indicates whether there is a dust storm on segment (s) of a given grid (g). If there is a dust storm, the $Is(s, g)$ is 1, otherwise, the $Is(s, g)$ is 0. According to Eqs. (4) and (5), the Asp_ds in 0.5° grids during the Martian year and EDL season were shown in Fig. 9.

(1) In Fig. 9a, the Asp_ds in Chryse's 1600 km radius ring in a whole Martian year ranged from 0–10.8% and showed spatial inhomogeneity. Acidalia, the north of Chryse's 1600 km radius ring, was the region where dust storm activity occurred most frequently, followed by Chryse, Tempe and Arabia, the east and west of the monitoring area. The Xanthe, the south of the Chryse, was the region with the lowest Asp_ds. While in the Chryse area (black polygon), the spatial probability of dust storm activity was also nonuniform featured with the fact that the probability was lower in the west and south but higher in the east and north. The Asp_ds in the Chryse area ranged from 0.19–2.42%, with an average of 1.22%.

In Fig. 9b, the Asp_ds of monitoring area during EDL season was the highest in the northern area (Acidacia) but it cut down little by little in the southern area and on both sides of the east and west. The dust storm activity probability in the north of Xanthe, east of Tempe and west of Arabia levelled off to 0, which was lower than that in a whole Martian year (Fig. 9a). It is because that the dust storm activity in the south of monitoring area mostly occurred in Ls = 135°-160° and 305°-340°, not during EDL season (Fig. 5). The Asp_ds in the Chryse area during EDL season ranged from 0.03–2.03%, with an average of

0.59%. The northeastern part of the Chryse area was featured with the highest Asp_ds, followed by the middle and western parts, while the eastern part had the lowest one.

(2) Asp_ds distribution in Chryse area can be explained from the following aspects:

(i) Topography. Guzewich et al. (2017) reported that there was an evident anti-correlation between Martian surface roughness from Digital Elevation Model (DEM) data and dust storm frequency (-0.32). In addition, there were two peaks near − 4 km and + 2 km in the histogram which displayed the dust storm frequency plotted against the Martian topography made by Guzewich et al (2017). Chryse lies on the east of Tempe, west of Arabia, north of Xanthe and south of Acidalia (Fig. 1b), a flat place with its elevation from − 4923 m to -2922 m. From Fig. 1b, it can be seen that the central and northern parts of the Chryse area are not hilly but relatively flat, and the terrain is more complex and the ground is rougher in other parts of Chryse. In addition, the elevation of Chryse's central and northern parts is the lowest, ranging from − 4030 m to -3850 m while the rest part of the Chyrse area is higher (-3800 m to -3200 m). Hence, the spatial probability of dust storm activity in Chryse's central and northern parts is greater than that in the rest part.

(ii) Dust storm activity Acidalia is an area where dust storm sequence occurs most intensively and Chryse is one of the origin areas of dust storm activity (Wang et al., 2015). Most of Chryse's 1600 km radius ring have previously been identified as the dust storm frequency According to Hinson and Wang (2010), the following factors can affect regional frontal/flushing dust storms in time and location: conversion among baroclinic wave modes; storm zones and standing waves. Mars general circulation model (MGCM) simulations stated clearly that Acidalia's wingward had intense surface stresses, showing no differences with these findings (Newman et al., 2002; Mulholland et al., 2013). As a result, the Chryse's northern and central parts were featured with higher spatial probability of dust storm activity.

(iii) Routes of dust storm In the northern hemisphere, three main paths existed from the north to the south, namely, through Acidalia, Utopia and Arcadia (Wang et al., 2015). The above-mentioned sequences entail numerous frontal/flushing dust storms in previous studies, the large proportion of which disperse in the northern hemisphere (Wang et al., 2005; Hinson and Wang, 2010). A branch of Acidalia sequences extends eastward in the southern low latitudes, through the Chryse area from east to west (Fig. 7a). Hence, the dust storm activity in space in the east is higher than that in the west, just as the probability in space in the north is higher than that in the south.

(3) Taking into account the spatial probability of dust storm activity and Chryse's topography, the flat 0.5° grids with lower probability can be selected as the preferred landing areas (PLAs). As shown in Fig. 9b, three PLAs (dotted rectangles marked with number 1–3) were labeled. The PLA 1 and 2 were in the west of Chryse area, while the PLA 3 was in its east. The area of three PLAs was 65856 km^2, 84744 km^2 and 70242 km^2 with an average Asp_ds of 0.45%, 0.26% and 0.03% during EDL season in respective.

Finally, based on the dust storm activity probability in time and space in the Chryse area during EDL season, we could draw a conclusion that Ls = 18°-65° can be chosen as the preferred landing time and

the three PLAs in Chryse as the preferred landing areas.

5 Spatial and seasonal pattern of dust storm activity in the Chryse area

EOF was firstly applied in geophysics by Lorenz (1956) and then had been used to analyze data with complex spatial and temporal characteristics. In view of EOF, the eigenfunctions, empirically found and best describing the information, could be regarded as the key to the most valid way to decompose data into representative patterns (Kaihatu et al., 1998). EOF analysis, one of the principal component analysis, can disassemble the spatiotemporal data set into a linear combination of spatial function and time function, so as to acquire dust storm spatial mode (the principal component) and the time projection (time series) associated. These independent spatial modes not only cover the dust storm information in the original study area, but also rank in line with the variance contribution. Hence, it is possible for us to distinguish and explain the dust storms types in the study area via the linear combination of the first several modes. In the light of dust storm frequency binned by 0.5° longitude and latitude of Chryse's 1600 km radius ring, it's reasonable for us to find out the leading and separate modes of dust storm in space arisen from the dust storm activity by aid of EOF. Each 0.5° grid could be regarded as a measuring point in the Chryse area which can be observed once a Martian day during four Martian years. The final observations could form a spatiotemporal data set of dust storms in the study area. The main purposes of using EOF to analyze Chryse's dust storm spatiotemporal data set are to: analyze the spatiotemporal data set of dust storms in the study area via EOF analysis to acquire the space-time distribution pattern of dust storm; carry out factor analysis concerned between dust storm modes and the factors affecting dust storms (the growth and retreat of the Arctic ice cap or the dust storms origin, etc.), acquiring the main types and explanations of dust storms in the study area. The results were shown in Figs. 10 and 11.

Figure 10a shows the variance bound up with every EOF pattern (the eigenvalues) of dust storm activity in the Chryse area. One Martian year can be divided into 36 segments binned by 10° of Ls, obtaining 36 EOF modes. It can be seen that the first mode and the second one account for 40.5% and 17.5% of the total variance separately, comprising 58% of the total variance associated with dust storm activity. However, mode 5–36 variance is very small. We deemed that Mode 1 and 2 possessed valuable information but higher-order modes may be caused by the stochastic noise.

The first two EOF modes for dust storm activity within Chryse's 1600 km radius ring are shown in Fig. 11. Mode 1 (Fig. 11a) is dominated by negative values in the north of the monitoring area, ranging from near 30°-57°N. There are weak positive values in the south of the monitoring area. Although Mode 2 (Fig. 11b) possesses the same spatial model as Mode 1, the negative values shifted southward to the bottom of the monitoring area, nearly. The highest positive values of Mode 2 occur in the north of the monitoring area. Mode 1 and 2 show enormous vertical variations from the north to the south in the monitoring area. In the northern half of the Chryse area, the two modes were arranged and located differently, but they obviously showed a near north-south frontal feature with the evident gradient.

Figure 11 Eigenvector image patterns for Mode 1 (a) and Mode 2 (b) of temporal variance within Chryse's 1600 km radius ring in 0.5° grids. The black polygon shows the Chryse area. The topographic map is

shown in black contours (2 km apart) for reference.

In Fig. 10c, Mode 2 also has obviously seasonal characteristics, with the positive values lasting mainly from the northern hemisphere spring to summer and negative values occurring in the rest of the Martian year. And the negative eigenvector values occur in the middle of the monitoring area, surrounded by positive values (Fig. 11b). We held that the Mode 2 was related to the native/textured dust storm activity. Textured dust storms with visible textures on cloud top are characterized by convection or turbulence. It is speculated that the vertical mixing related to shear cut or convection taking place in the dust column and the texture develops on the dust storm top with the occurrence of lifting (e.g., Strausberg et al., 2005; Guzewich et al., 2015). When the dust ceased, it began to mix and spread horizontally, making the texture smooth until the obviously textured dust storm dissipates. Untextured storms were the dissipation stage of textured ones. According to four Martian years' MOC MDGMs, there were 764 textured dust storms out of 1172 previously identified dust storms. The daily number of textured dust storm within 1600 km radius monitoring area was shown in Fig. 10e. Based on Fig. 10c and e, we discovered that Mode 2 had a negative correlation with the daily frequency of textured dust storm within the monitoring area. The three daily frequency peaks (7 at Ls = 18°, 15 at Ls = 220° and 21 at Ls = 316°) of textured dust storm (Fig. 10e) were consistent with the negative values of Mode 2 (Fig. 10c). While during Ls = 100°-110°, the number of textured dust storms has reduced to 0, which was in accord with positive values of Mode 2 in Fig. 10c. Thus, it could be concluded that around 17.5% of the dust storm activity variance within Chryse's 1600 km radius can be interpreted as Mode 2, which was recognized as textured dust storm.

6 Summaries

Tianwen-1 mission is scheduled to launch in 2020 with the goals of "orbiting, landing and roving". Two tentative landing areas (Chryse and Isidis) were selected in the latitude range of 5°-30° (Fig. 1a). The precision and success during EDL season for a Martian landing mission is affected by local atmospheric conditions, especially the dust storm probability. Therefore, it's critical to China's 2020 Mars Mission to detect the possibilities and characteristics of dust storm activities in and around Chryse by aid of remote sensing imagery collected over multiple Martian years.

This paper tends to use the images of MOC MGS to calculate the daily mean dust storm probability within 1600 km radius ring of the Chryse area by 1° of solar longitude to find out the appropriate period and compute the mean occurrence probability of dust storm in space during EDL season and a whole Martian year to discover the suitable landing areas. The results are as follows:

(1) Adp_ds in the Chryse area (blue color) and within its 1600 km radius ring (red color) peaked at 42.9% (Ls = 223°) and 20.9% (Ls = 225°), respectively. The minimum of Adp_ds in Chryse monitoring area is 0. Adp_ds in the Chryse area and within its 1600 km radius ring showed obvious in-homogeneity and seasonality within a Martian year. In the Chryse area, dust storm activity was the most frequent from the northern hemisphere autumnal equinox (Ls = 177°) to the end of autumn (Ls = 239°), with an average Adp_ds of 9.5%. The optical depth measurements obtained by the Spirit Rover was related to storm

activity observations in the Chryse area and its 1600 km radius ring, except for the first peak (Ls = 160°). Dust storm activity in Chryse monitoring area was mainly centered in the period from Ls = 180° to Ls = 240° and thus we deemed that these storms were resulted from the Acidalia-Chryse channel.

(2) The latitudinal distribution of dust storm center in the monitoring area by 1° of Ls (Fig. 5) showed seasonal and spatial heterogeneity. Firstly, the frequency of dust storm activity was closely related to the seasonal waxing and waning of the arctic polar ice cap. Dust storms within Chryse's 1600 km radius ring mostly arose during the growth or the regression of the polar cap rather than its quiescent stage when the cap's change rate approached to the minimum. In the northern hemisphere, the dust storm activity at the edge of cap almost was at a standstill before or on the North Summer Solstice, and this stagnation lasted for a long time (Ls = 20°- 80°). Secondly, the dust storm activity within the monitoring area mainly came from the arctic polar cap region, Acidalia and Chryse, and a small numbers were from the southern hemisphere (Argyre and Bosprous) which travelled northward. Nevertheless, the dust storms from the southern hemisphere were much smaller and much less frequent than the ones from the northern hemisphere.

(3) The Asp_ds in Chryse's 1600 km radius ring ranged from 0–10.8% and showed spatial in-homogeneity. Acidalia, the north of Chryse's 1600 km radius ring, was the region where dust storm activity occurred most frequently, followed by Chryse, Tempe and Arabia, the east and west of the monitoring area. The Asp_ds of monitoring area during EDL season was the highest in the northern area (Acidacia) but it cut down little by little in the southern area and on both sides of the east and west. The dust storm activity probability in the north of Xanthe, east of Tempe and west of Arabia levelled off to 0, which was lower than that during the MY. The nonuniform Asp_ds distribution can be explained by three factors: topography, the origin and the route of dust storm sequences.

(4) In EDL season, dust storm lasted during Ls = 345°-3° and 13°-18° in the Chryse area, which was not the time for landing mission. However, dust storm activity was found in only five sols during Ls = 18°-65°, with the Adp_ds being less than or equal to 1.6% and an average of 0.15%. As shown in Fig. 9b, three PLAs (dotted rectangles marked with number 1–3) were labeled. The PLA 1 and 2 were in the west of the Chryse area, while the PLA 3 lied in its east. The area of three PLAs was 65856 km^2, 84744 km^2 and 70242 km^2 on the whole with an average Asp_ds of 0.45%, 0.26% and 0.03% during EDL season, respectively. According to the temporal and spatial probability of dust storm activity in the Chryse area during EDL season, we held that the preferred landing time of Tianwen-1 mission in 2021 was in Ls = 18°-65° and three preferred landing areas were selected with low dust storm probability.

(5) It's reasonable for us to find out the leading and separate modes of dust storm in space by aid of EOF. The first mode and the second one have 40.5% and 17.5% of the total variance separately, comprising 58% of the total variance associated with dust storm activity. Mode 1 and 2 show enormous vertical variations from the north to the south in the monitoring area. In the northern half of the Chryse area, the two modes are arranged and located differently, but they obviously show a near north-south frontal feature with the evident gradient. Mode 1 is primarily consistent with the seasonal growth and regression

of the arctic polar cap edge, thus 40.5% of annual dust storm activity within Chryse's 1600 km radius ring can be regarded as the cap edge storm in the northern hemisphere. Mode 2 has an approximate negative correlation with the daily frequency of textured dust storm within the monitoring area. Thus, it could be concluded that around 17.5% of the dust storm activity variance within Chryse's 1600 km radius can be interpreted as Mode 2, which was recognized as textured dust storm.

Abbreviations

EDL
Entry-Descent-Landing; MOC:Mars Orbiter Camera; MDGMs:Mars Daily Global Maps; EOF:Empirical orthogonal function; MGS:Mars Global Surveyor; MOLA:Mars orbit laser altimeter; WA:wide-angle; PEDE:planet encircling dust event; DEM:Digital Elevation Model; MGCM:Mars general circulation model; PLAs:the preferred landing areas.

Declarations

Acknowledgements

The efforts of the science and engineering teams behind all the data sets used in this study, particularly the MGS mission, MOC WA instruments, are gratefully acknowledged.

Authors' contributions

B.L. and S.B.C designed the research. B.L. wrote the manuscript and performed calculations. P.W.Y., C.F.L., J.Z. and Z.Y.Y contributed to the data processing and science interpretations. X.H.F and B.W contributed to the geological interpretations of the data. Z.C.L and X.H.F helped to process the MDGMs data and manuscript preparations. All authors have approved the final version of the manuscript.

Funding

This work is supported by the Strategic Leading Science and Technology Special Project of Chinese Academy of Sciences (XDB41000000), the Shandong Provincial Natural Science Foundation (ZR2019MD015), the National Natural Science Foundation of China (U1931211), the Pre-research project on Civil Aerospace Technologies No. D020102 funded by China National Space Administration (CNSA).

Availability of data and materials

All MOC images for this research are available in Harvard Dataverse: https://doi.org/10.7910/DVN/WWRT1V.

Competing interests

The authors declare that they have no competing interests regarding this document.

References

1. Benson JL, James PB (2005) Yearly comparisons of the martian polar caps: 1999–2003 Mars Orbiter Camera observations. Icarus 174:513–523
2. Briggs GA, Baum WA, Barnes J (1979) Viking orbiter imaging observations of dust in the martian atmosphere. J Geophys Res 84:2795–2820
3. Calvin WM, James PB, Cantor BA, Dixon EM (2015) Interannual and seasonalchanges in the north polar ice deposits of Mars: Observations from MY 29–31 usingMARCI. Icarus 251:181–190. https://doi.org/10.1016/j.icarus.2014.08.026
4. Cantor BA (2007) Moc observations of the 2001 mars planet-encircling dust storm. Icarus 186(1):60–96
5. Cantor BA, James PB, Caplinger M, Wolff MJ (2001) Martian dust storms: 1999 Mars orbiter camera observations. J Geophys Res 106(E10):23653–23687
6. Cantor BA, Pickett NB, Malin MC, Lee SW, Wolff MJ, Caplinger MA (2019) Martian dust storm activity near the mars 2020 candidate landing sites: mro-marci observations from mars years 28–34. Icarus
7. Cantor BA, Wolff MJ, James PB, Higgs E (1998) Recession of the Martian north polar cap: 1990–1997 Hubble Space Telescope observations. Icarus 136:175–191
8. Gifford FA (1964) A study of Martian yellow clouds that display movement. Mon Weather Rev 92:435–440
9. Guzewich SD, Toigo AD, Kulowski L, Wang H (2015) Mars Orbiter Camera climatology of textured dust storms. Icarus 258:1–13. http://doi.org/10.1016/j.icarus.2015.06.023
10. Guzewich SD, Toigo AD, Wang H (2017) An investigation of dust storms observed with the mars color imager. Icarus 289:199–213
11. Desai PN, Knocke PC (2007) Mars exploration rovers entry, descent, and landing trajectory analysis. J Astronaut Sci 55, 311–323. https://doi.org/10.1007/ BF03256527
12. Heavens NG, McCleese DJ, Richardson MI, Kass DM, Kleinböhl A, Schofield JT (2011) Structure and dynamics of the Martian lower and middle atmosphere as observed by the Mars climate sounder: 2. Implications of the thermal structure and aerosol distributions for the mean meridional circulation. J Geophys Res 116:E01010. doi:10.1029/2010JE003713
13. Hinson DP, Wang H (2010) Further observations of regional dust storms andbaroclinic eddies in the northern hemisphere of Mars. Icarus 206(1):290–305. http://dx.doi.org/10.1016/j.icarus.2009.08.019
14. Hollingsworth JL, Haberle RM, Schaeffer J (1979) Seasonal variations of storm zoneson Mars. Adv Space Res 19:1237–1240
15. James PB, Martian local dust storms, in Recent Advances in Planetary Meteorology, edited by G. Hunt, pp. 85–100, Cambridge Univ. Press, New York, 1985
16. James PB, Cantor BA (2001) Martian north polar cap regression: 2000 Mars Orbiter Camera observations, Icarus, 154, 131–144

17. Kaihatu JM, Handler RA, Marmorino GO, Shay LK (1998) Empirical orthogonal function analysis of ocean surface currents using complex and real-vector methods. J Atmos Ocean Technol 15(4):927–941
18. Lemmon MT, Wolff MJ, Bell JFIII, Smith MD, Cantor BA, Smith PH (2015) Dustaerosol, clouds, and the atmospheric optical depth record over 5 Mars years of the Mars Exploration Rover mission. Icarus 251:96–111. http://dx.doi.org/10.1016/j.icarus.2014.03.029
19. Leovy CE, Zurek RW, Pollack JB (1973) Mechanisms for Mars dust storms. J Atmos Sci 30:749–762. doi:10.1175/1520-0469(1973)0300749:MFMDS2.0.CO;2
20. Lorenz E (1956) Empirical orthogonal functions and statisticalweather prediction. In: Tech. Rep. 1, Statistical Forecasting Project,Department of Meteorology. Massachusetts Institute of Technology, Cambridge, 49 pp
21. Malin MC, Danielson GE, Ingersoll AP, Masursky H, Veverka J, Ravine MA, Soulanille TA (1992) The Mars Observer Camera. J Geophys Res 97:7699–7718
22. Martin LJ (1974) The major martian dust storms of 1971 and 1973. Icarus 23:108115
23. Martin LJ (1976) 1973 dust storm: Maps from hourly photographs. Icarus 29:363–380
24. Martin LJ, Zurek RW (1993) An analysis of the history of dust storm activity on Mars. J Geophys Res 98:3221–3246
25. Martin-Mur TJ, Kruizingas GL, Burkhart PD, Wong MC, Abilleira F (2012) Mars science laboratory navigation results. In: 23rd International Symposium Space Flight Dynamics, 43257. Pasadena, California
26. Miyamoto S (1957) The Great Yellow Cloud and the Atmosphere of Mars: Report of Visual Observations During the 1956 Opposition. Contrib. Inst. Astrophys. Kwasan Obs., No. 71
27. Mulholland DP, Read PL, Lewis SR (2013) Simulating the interannual variability ofmajor dust storms on Mars using variable lifting thresholds. Icarus 223:344–358
28. Newman CE, Lewis SR, Read PL, Forget F (2002) Modeling the martian dustcycle. 2. Multiannual radiatively active dust transport simulations. J GeophysRes 107. http://dx.doi.org/10.1029/2002JE001920
29. Peijian YE, Zezhou S, Wei R, Linzhi M (2017) Mission overview and key technologies of the first, mars probe of China. Sci China Tech Sci, 2017, 60
30. Peterfreund AR, Kieffer HH (1979) Thermal infrared properties of the martian atmosphere. 3. Local dust storms. J Geophys Res 84:2853–2863
31. Ryan JA, Henry RM (1979) Mars atmospheric phenomena during major dust storms, as measured at surface. J Geophys Res 84:2821–2829
32. Ryan JA, Sharman RD (1981) Two major dust storms, one Mars year apart: Comparison from Viking data. J Geophys Res 86:3247–3254
33. Shirley JH, Mischna MA (2017) Orbit-spin coupling and the interannual variability of global-scale dust storm occurrence on mars. Planetary Space Science 139:37–50

34. Smith MD (2004) Interannual variability in TES atmospheric observations of mars during 1999–2003. Icarus 167:148–165
35. Strausberg MJ, Wang H, Richardson MI, Ewald SP, Toigo AD (2005) Observations of the initiation and evolution of the 2001 Mars global dust storm. JGeophys Res 110:E02006. doi:10.1029/2004JE002361
36. Tamppari LK, Barnes J, Bonfiglio E, Cantor BA, Friedson AJ, Ghosh A, Grover MR, Kass D, Martin TZ, Mellon M, Michaels T, Murphy J, Rafkin SCR, Smith MD, Tsuyuki G, Tyler D, Wolff M (2008) Expected atmospheric environment for the Phoenix landing season and location. J Geophys Res 113(E00A23). https://doi.org/10.1029/2007JE003039
37. Toigo AD, Richardson MI, Wilson RJ, Wang H, Ingersoll AP (2002) A first lookat dust lifting and dust storms near the south pole of Mars with a mesoscalemodel. J Geophys Res 107 (E7). doi:10.1029/2001JE001592
38. Vasavada AR, Chen A, Barnes JR, Burkhart PD, Cantor BA, Dwyer-Cianciolo AM, Fergason RL, Hinson DP, Justh HL, Kass DM, Lewis SR, Mischna MA, Murphy JR, Rafkin SCR, Tyler D, Withers PG (2012) Assessment of environments for mars science laboratory entry, descent, and surface operations. Space Sci Rev 170:793–835. https://doi.org/10.1007/s1121401299113
39. Wang H (2007) Dust storms originating in the northern hemisphere during thethird mapping year of Mars Global Surveyor. Icarus 189(2):325–343. http://dx.doi.org/10.1016/j.icarus.2007.01.014
40. Wang H, Fisher JA (2009) North polar frontal clouds and dust storms on Marsduring spring and summer. Icarus 204(1):103–113. doi:10.1016/j.icarus.2009.05.028
41. Wang H, Ingersoll AP (2002) Martian clouds observed by Mars Global Surveyor Mars Orbiter Camera. J Geophys Res 107 (E10), 5078. doi:10.1029/ 2001JE001815
42. Wang H, Richardson MI, Wilson RJ, Ingersoll AP, Toigo AD (2003) Cyclones,tides, and the origin of a cross-equatorial dust storm on Mars
43. Wang H, Richardson MI (2015) The origin, evolution, and trajectory of large dust storms on mars during mars years 24–30 (1999–2011). Icarus 251:112–127
44. Wang H, Zurek RW, Richardson MI (2005) Relationship between frontal duststorms and transient eddy activity in the northern hemisphere of Mars asobserved by Mars Global Surveyor. J Geophys Res 110:E7. http://dx.doi.org/10.1029/2005JE002423
45. Zurek RW, Martin LJ (1993) Interannual variability of planet-encircling dust storms on Mars. J Geophys Res 98:3247–3259

Figures

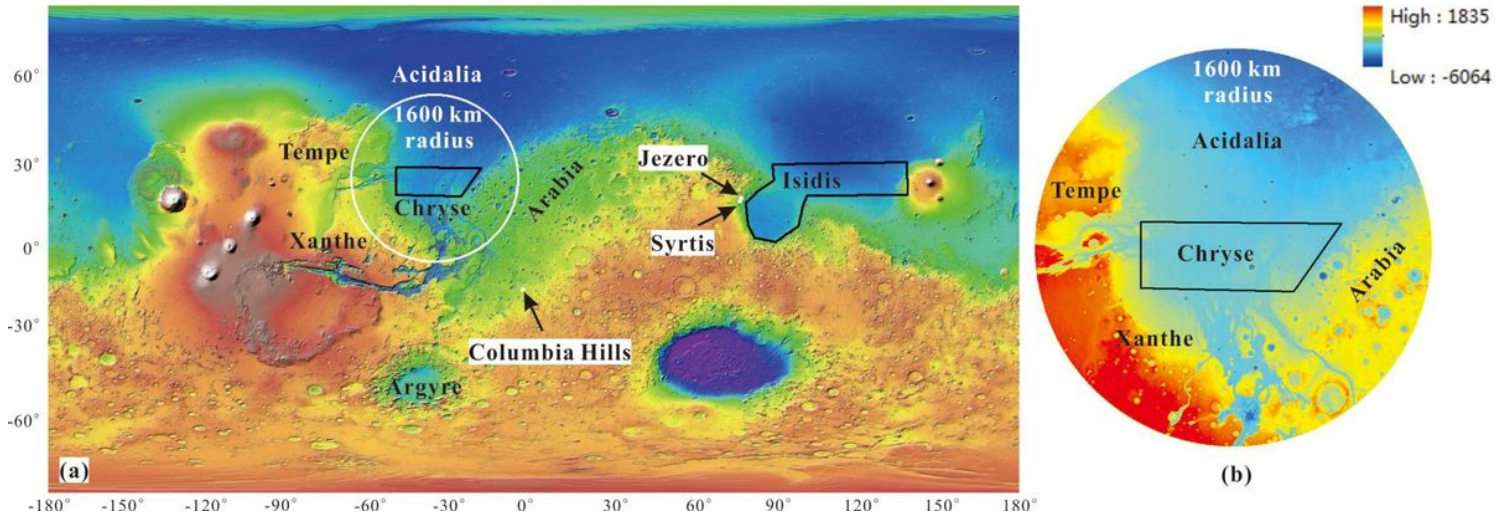

Figure 1

(a) Two tentative landing areas of Tianwen-1 mission in elevation rendering map from Mars Global

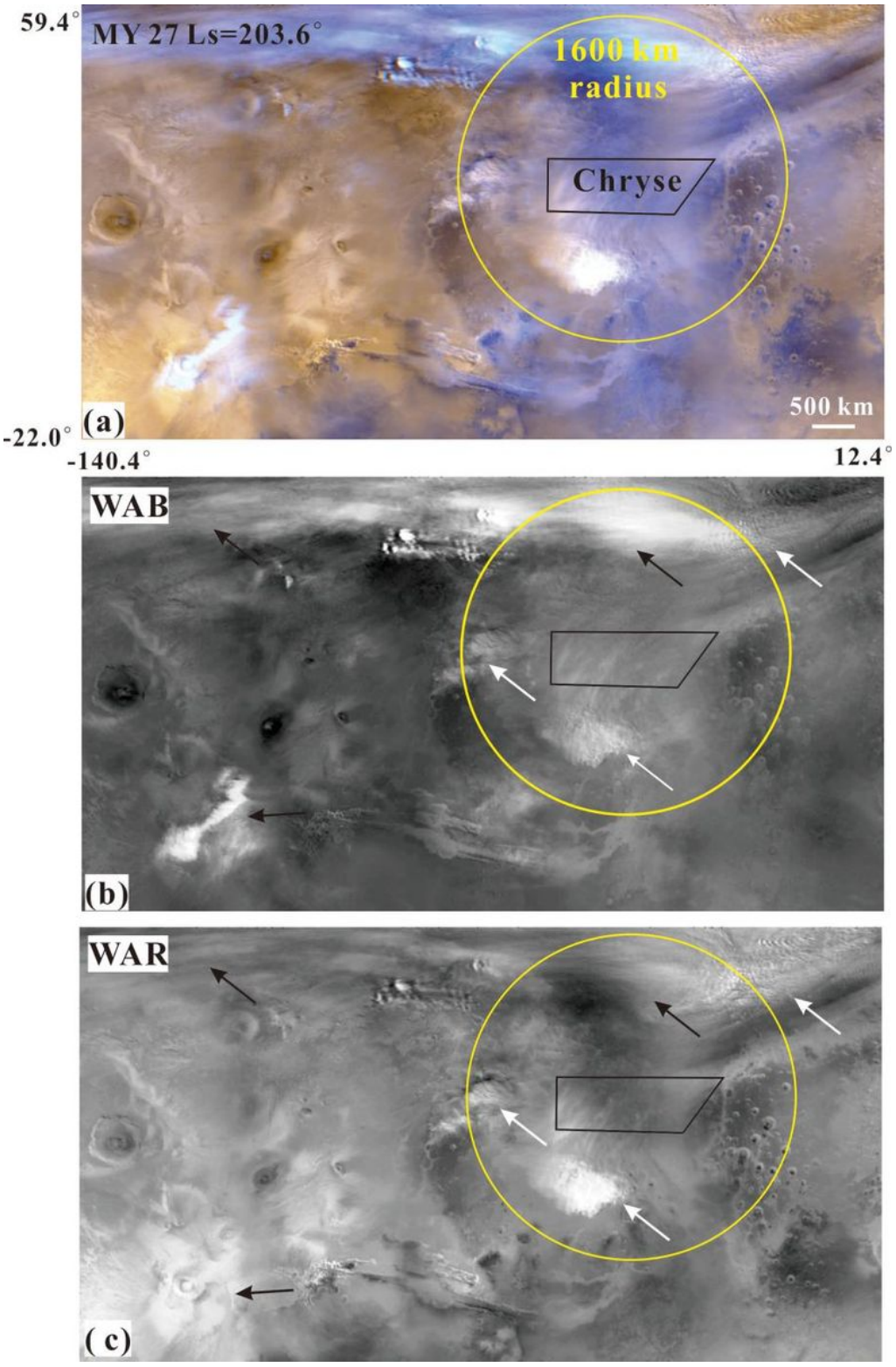

Figure 2

(a) Example of a MOC MDGM section (MY 27, Ls=203.6°) in the Chryse area. (b) and (c) are the blue and red bands of this image. These two absorber views could discriminate between clouds (black arrows) and dust storm activity (white arrows). The black polygon and yellow circle are the Chryse area and its 1600 km radius monitoring ring, respectively.

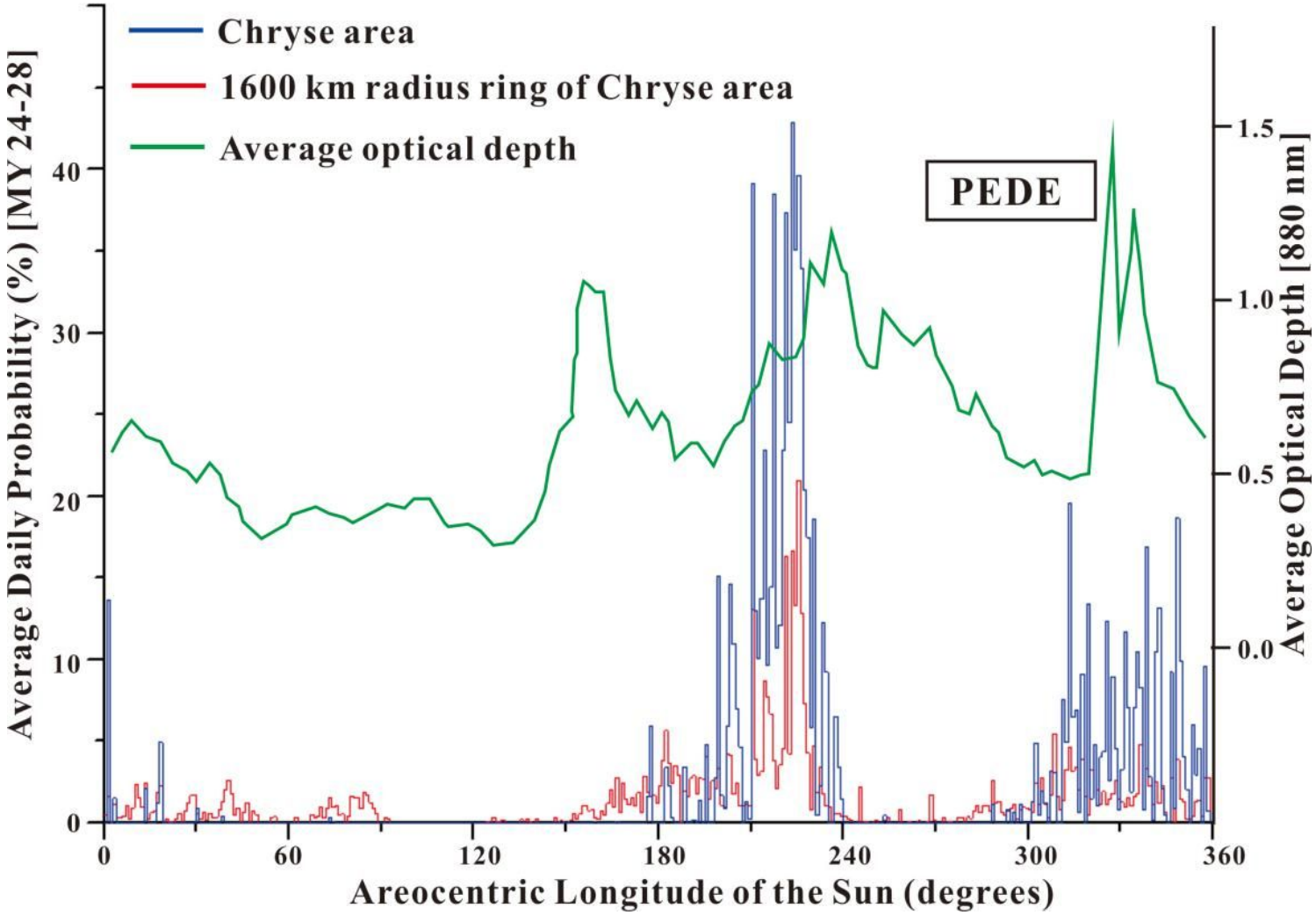

Figure 3

Daily mean dust storm frequency is proportional to Ls of the Chryse area (blue color) and within its 1600 km radius ring (red color) in 1° of Ls. The green curve shows the average optical depth gauged by the Spirit Rover (Lemmon et al., 2015) in 2.5° of Ls, eliminating the responses of the PEDE in MY 29.

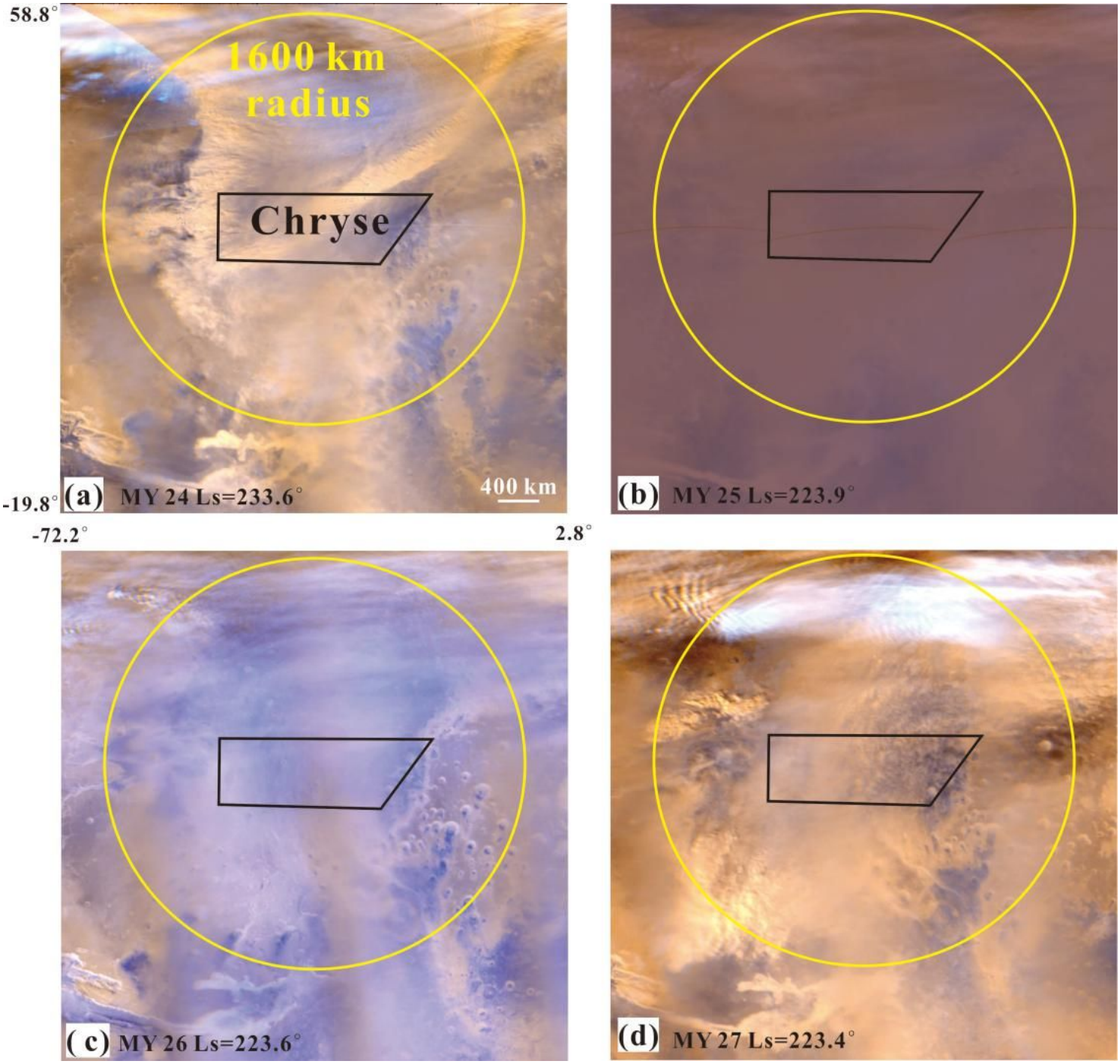

Figure 4

The MOC MDGMs at Ls=223° of Chryse area in four Martian years. The black polygon and yellow circle are the Chryse and its 1600 km radius monitoring ring.

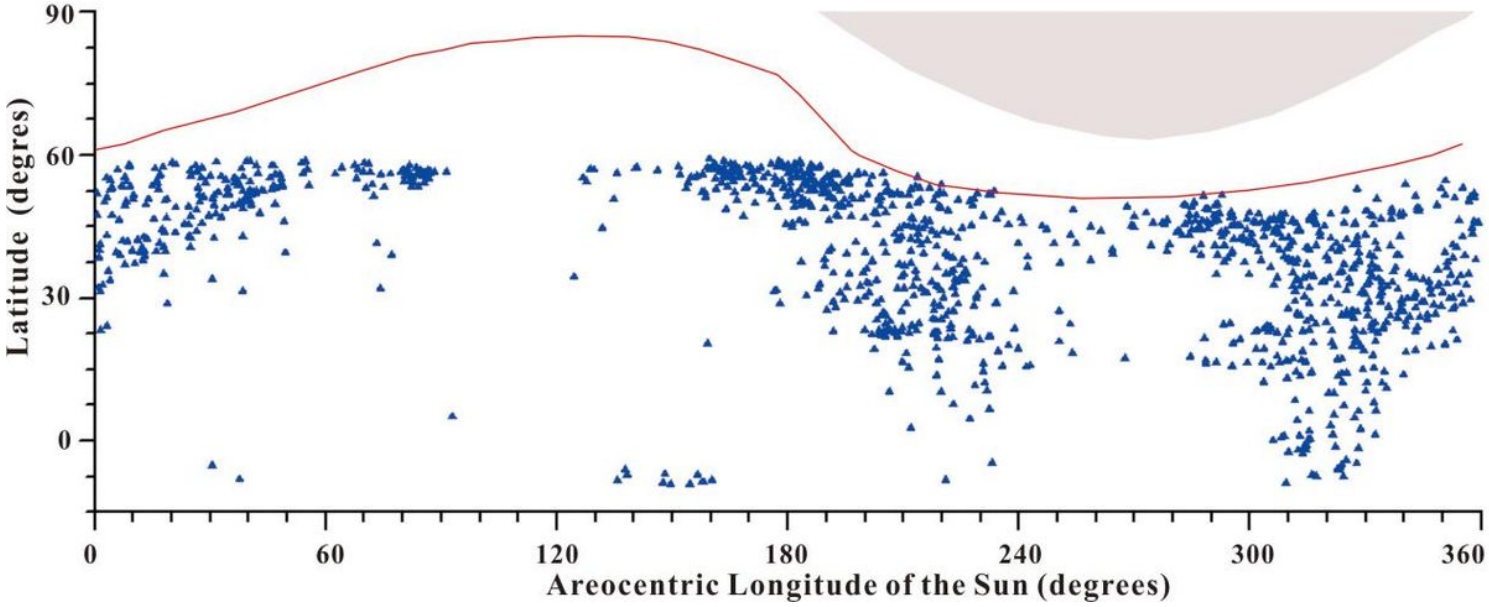

Figure 5

Dust storm latitude distribution, observed within Chryse's 1600 km radius ring, being proportional to Ls=1°. The red curve indicates the mean latitude of the arctic polar cap edge, while gray area at the top shows the terminator. The blue triangles are the centers of dust storm events.

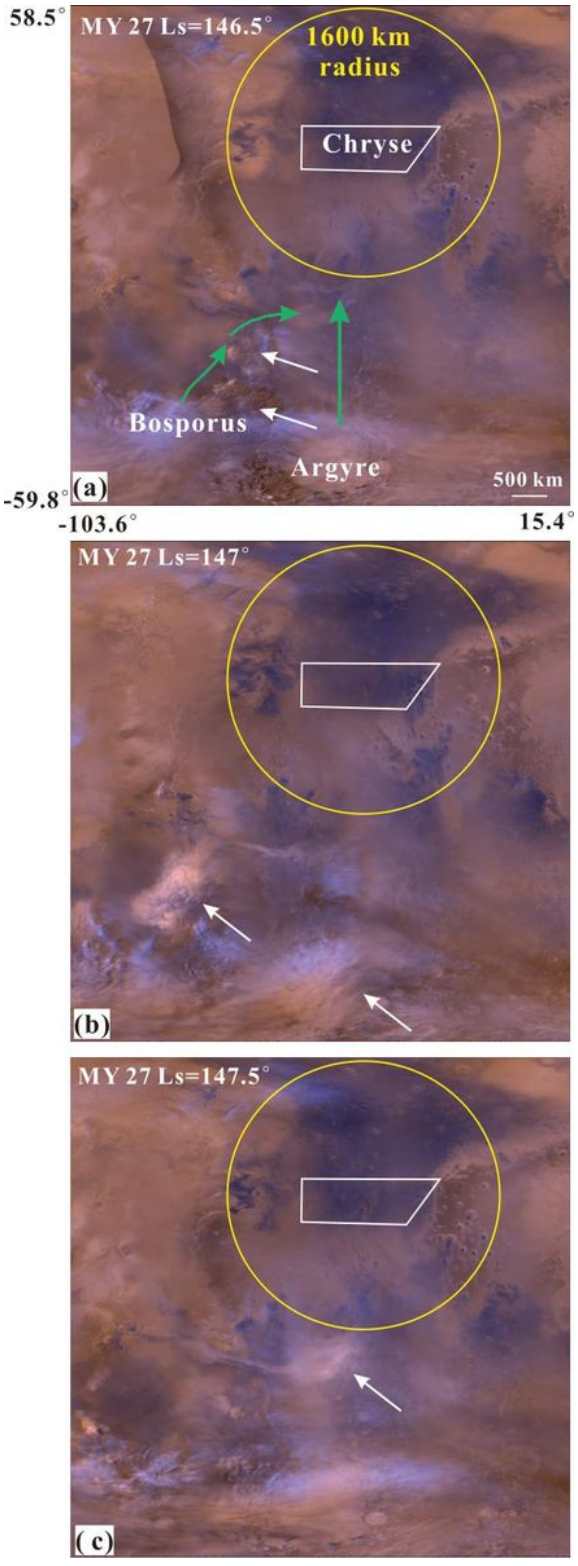

Figure 6

The dust storm activity of the southern hemisphere (Argyre and Bosporus) in northern summer season (Ls=135°-160°) within the monitoring area of Chryse. (a), (b) and (c) are MOC MDGMs at Ls=146.5°-147.5° of MY 27, a simple cylindrical projection with a resolution of 6 km/pixel. The white and green arrows denote the dust storm events and the southern dust storm sequences (Wang et al., 2015),

respectively. The white polygon and yellow circle represent the Chryse area and its 1600 km radius monitoring area.

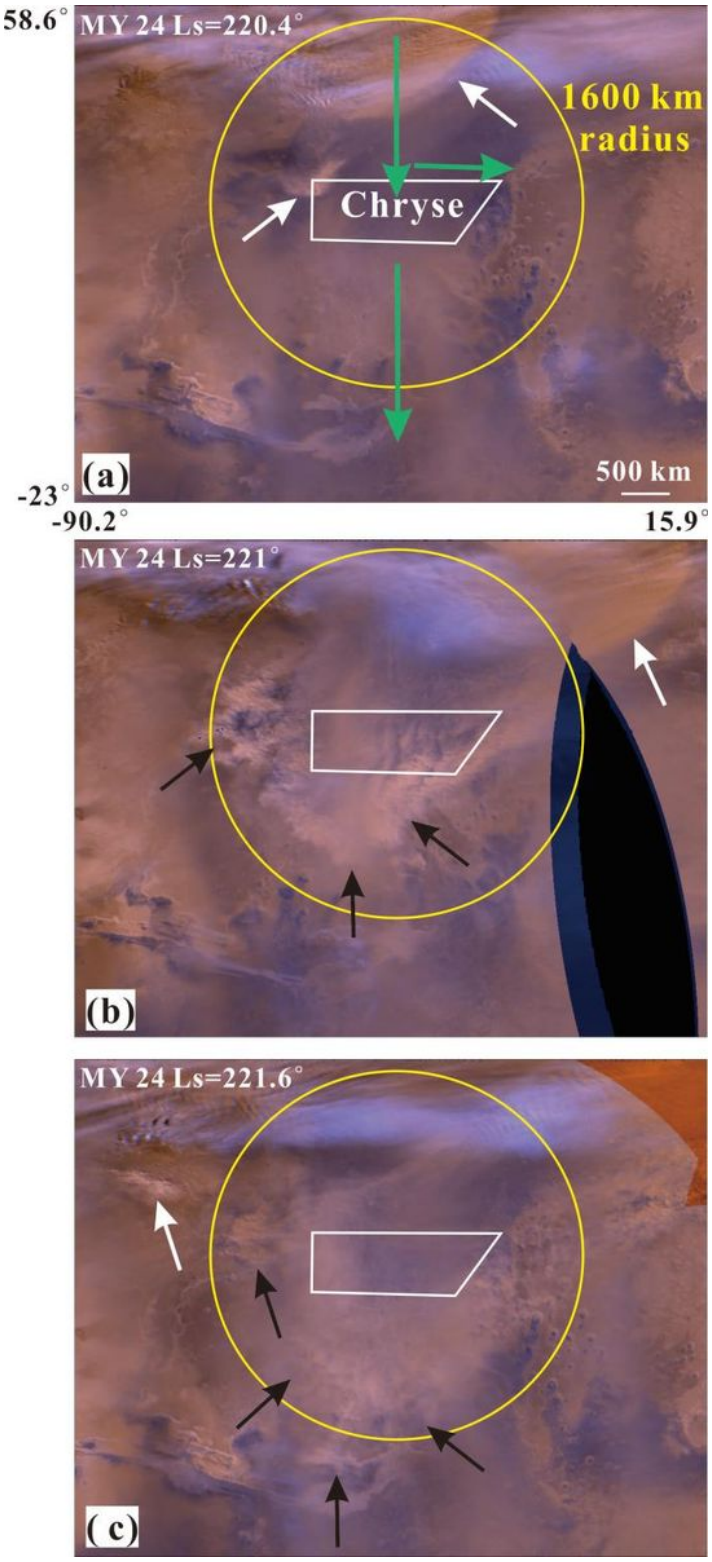

Figure 7

The dust storm activity in northern hemisphere autumn (Ls=180°-250°) within 1600 km radius ring of the Chryse area. (a), (b) and (c) are MOC MDGMs at Ls=220.4°-221.6° of MY 24, a simple cylindrical projection with a resolving power of 6 km/pixel. The white, black and green arrows are the native,

frontal/flushing dust storm event and the northern Acidalia dust storm sequences (Wang et al., 2015), respectively. The white polygon and yellow circle represent the Chryse area and its 1600 km radius monitoring area.

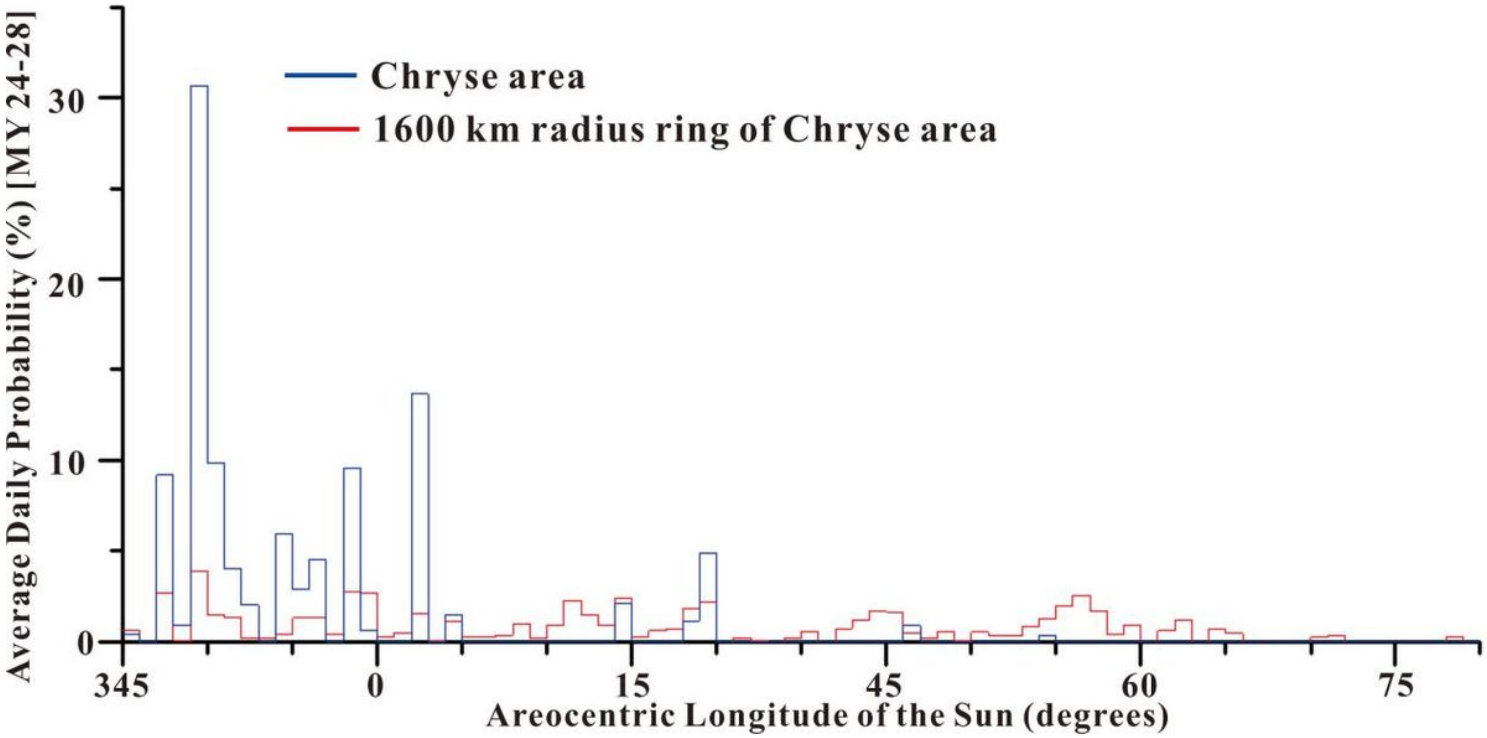

Figure 8

Daily mean dust storm probability in the Chryse area (blue color) and within its 1600 km radius ring (red color) between Ls=345°-65° (EDL season) with the increment of Ls=1° .

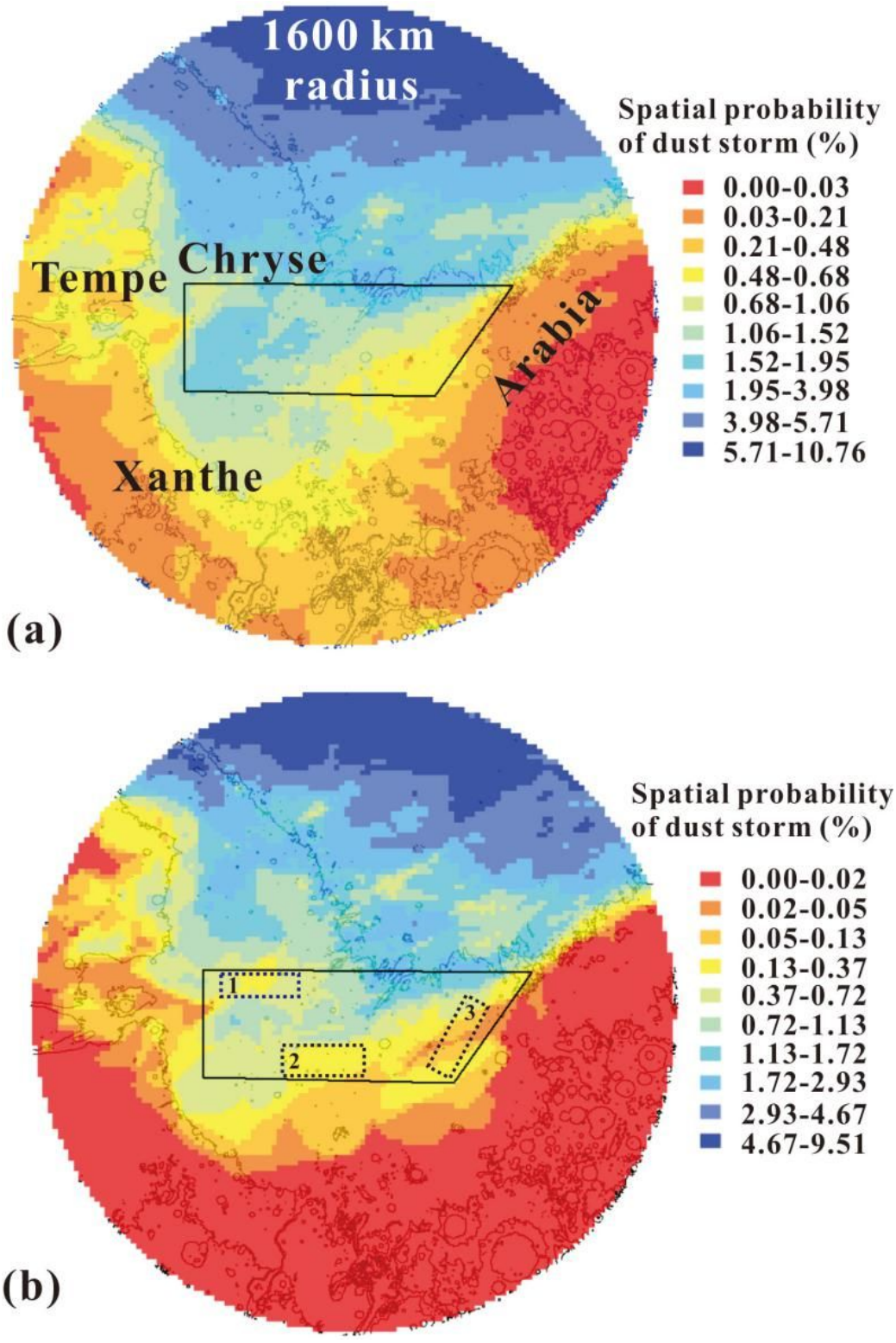

Figure 9

The dust storm activity probability in space within Chryse's 1600 km radius ring in MY (a) and EDL season (b) in each 0.5° grid. The black polygon shows the Chryse area. Topography is shown with black contours (2 km interval) for reference. The dotted rectangles marked with number 1-3 are the PLAs.

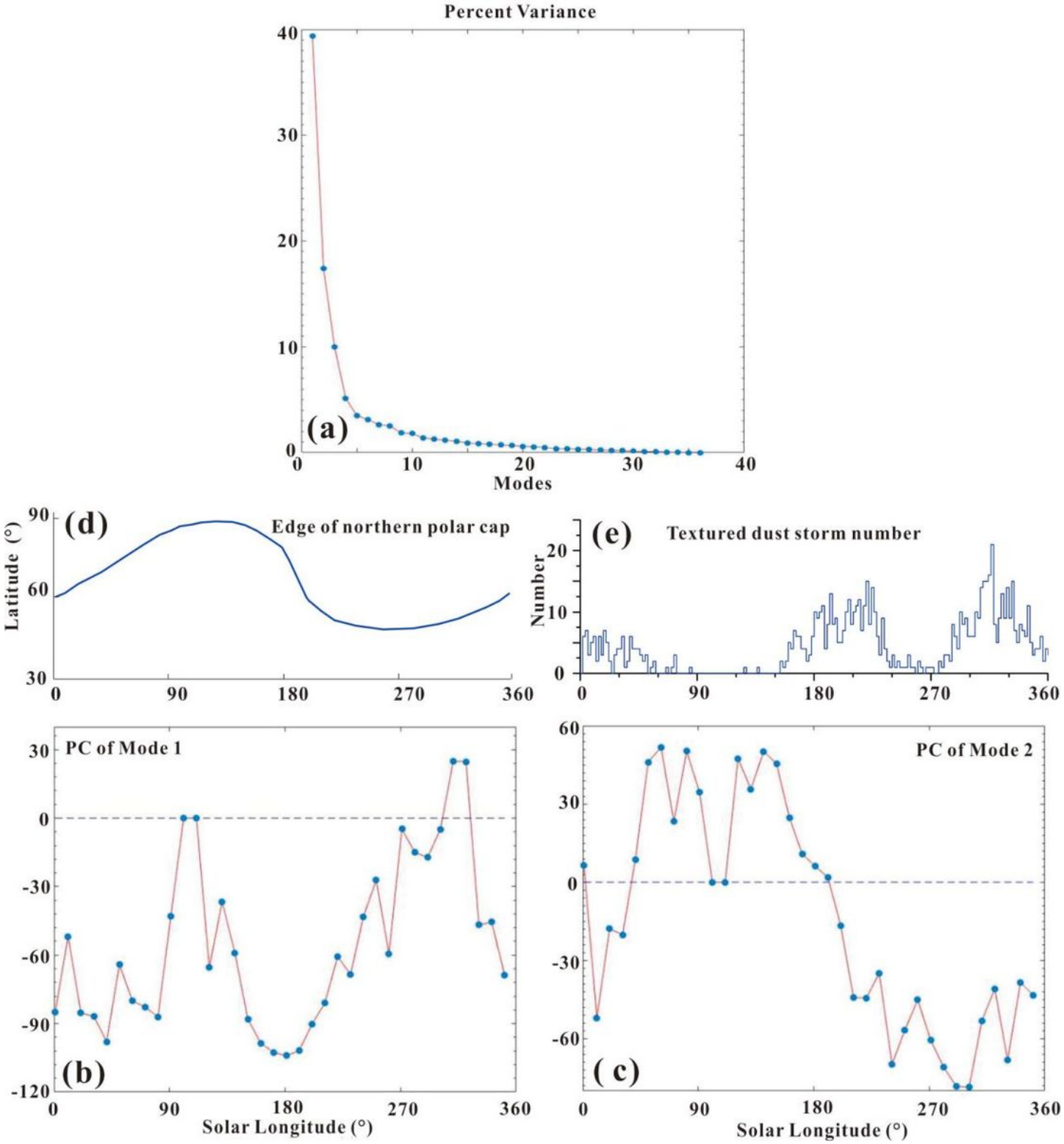

Figure 10

(a) The total variance percentage in dust storm activity within 1600 km radius ring of Chryse interpreted by every EOF mode. The principal components of EOF Mode 1 (b) and Mode 2 (c) demonstrate those modes' seasonality. (d) The average latitude of the arctic polar cap edge in its respective seasons. (e) The daily number of textured dust storm within Chryse's 1600 km radius ring.

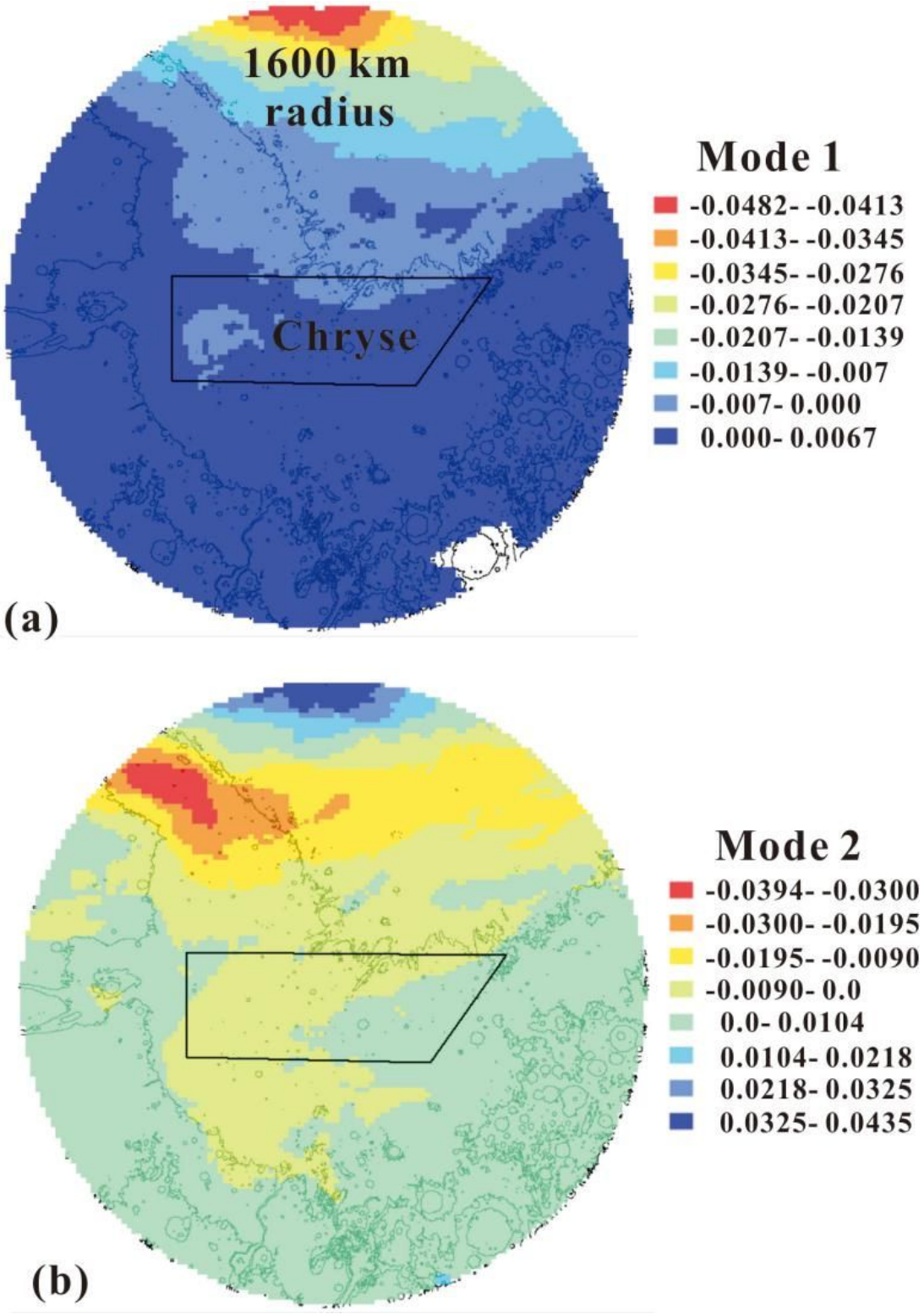

Figure 11

Eigenvector image patterns for Mode 1 (a) and Mode 2 (b) of temporal variance within Chryse's 1600 km radius ring in 0.5° grids. The black polygon shows the Chryse area. The topographic map is shown in black contours (2 km apart) for reference.

Supplementary Files

This is a list of supplementary files associated with this preprint. Click to download.

- GraphicalAbstract.docx